Journal of Magnetism and Magnetic Materials 528 (2021) 167817

Contents lists available at ScienceDirect

Journal of Magnetism and Magnetic Materials

journal homepage: www.elsevier.com/locate/jmmm

Combined effect of demagnetization field and magnetic anisotropy on magnetocaloric behavior and magnetocaloric-magnetoresistance correlation in GdTmErCoAl high-entropy amorphous alloy

Mingjuan Cai [a], Qiang Luo [a,*], Qiaoshi Zeng [a], Baolong Shen [a,b,*]

[a] School of Materials Science and Engineering, Jiangsu Key Laboratory of Advanced Metallic Materials, Southeast University, Nanjing 211189, China
[b] Institute of Massive Amorphous Metal Science, China University of Mining and Technology, Xuzhou 221116, China

ARTICLE INFO

Keywords:
Magnetocaloric effect
Magnetoresistance
Anisotropy
High-entropy amorphous alloy

ABSTRACT

The magnetic, magnetocaloric and transport properties were investigated systematically on $Gd_{20}Tm_{20}Er_{20}Co_{20}Al_{20}$ high-entropy amorphous ribbons with magnetic fields parallel and perpendicular to ribbon surfaces. It is found that the alloy shows greater magnetic entropy change and refrigeration capacity with maximum values of 9.7 J kg^{-1} K^{-1} and 551.3 J kg^{-1} under the perpendicular field change of 5 T, respectively, than those of 8.4 J kg^{-1} K^{-1} and 458.1 J kg^{-1} under the parallel field, respectively. This large difference cannot be simply understood from the demagnetization effect and indicates a significant role of magnetic anisotropy associated with the anisotropy of atomic packing. Besides, magnetoresistance and magnetic entropy change are found to have a power-law correlation with distinct power exponents in different sample orientations with respect to the field. Present results have implications for the understanding and design of amorphous refrigerants with advanced magnetocaloric performance.

1. Introduction

As promising substitutes for conventional gas refrigerants, magnetic refrigerants utilizing magnetocaloric effect (MCE) have arisen worldwide scientific and technological interest due to advantages of environmental friendliness and high efficiency [1–3]. A wide range of magnetocaloric materials has been explored to seek potential candidates for magnetic refrigeration in the sub-room temperature regime [4–6], which is of significance for gas-liquefaction applications. Excellent MCE in the sub-room temperature regime has been reported in rare earth (RE) based intermetallic compounds [7,8]. It has been suggested that RE-based amorphous alloys are also attractive for application as magnetic refrigerants due to their good MCE with negligible hysteresis losses and broad working temperature range [9–13]. And considerable efforts have been dedicated to understanding and enhancing the MCE of RE-based amorphous alloys by composition design and annealing [14–17]. Recently, the concept of high entropy (HE) [18–20] was introduced into the design of amorphous alloy. And a series of HE amorphous alloys with notably improved properties and unique characteristics were developed and explored [21–26], some of which showed good MCE. It is suggested that the strong chemical disorder resulted from the high configuration entropy leads to a sluggish magnetic transition over a wide temperature range and contributes to an enhanced refrigeration capacity (RC) [27–29]. Despite growing knowledge about the MCE of HE amorphous alloys, elusive atomic structure and high configuration entropy make the nature of magnetic dynamics and magnetocaloric behavior along with its relationship with other properties such as magnetoresistance (MR) poorly understood.

In addition, throughout the literature about the MCE of amorphous alloy ribbons, a determination of the effect of magnetic anisotropy on MCE and MR is almost missing. This is because amorphous alloys are usually thought to have isotropic MCE properties. Recently, the demagnetizing factor was found to have obvious impact on the magnetocaloric behavior of amorphous alloys [30–32]. In this manuscript, we further uncover that in addition to the demagnetization field, magnetic anisotropy associated with the structural anisotropy has marked effects on the magnetization, MCE and MR properties in the $Gd_{20}Tm_{20}Er_{20}Co_{20}Al_{20}$ HE amorphous alloy. Moreover, a power-law correlation between MR and magnetic entropy change (ΔS_M) is found within the measured temperature range, but demonstrates distinct

* Corresponding authors at: School of Materials Science and Engineering, Jiangsu Key Laboratory of Advanced Metallic Materials, Southeast University, Nanjing 211189, China (B. Shen).
E-mail addresses: q.luo@seu.edu.cn (Q. Luo), blshen@seu.edu.cn (B. Shen).

https://doi.org/10.1016/j.jmmm.2021.167817
Received 24 September 2020; Received in revised form 6 January 2021; Accepted 28 January 2021
Available online 15 February 2021

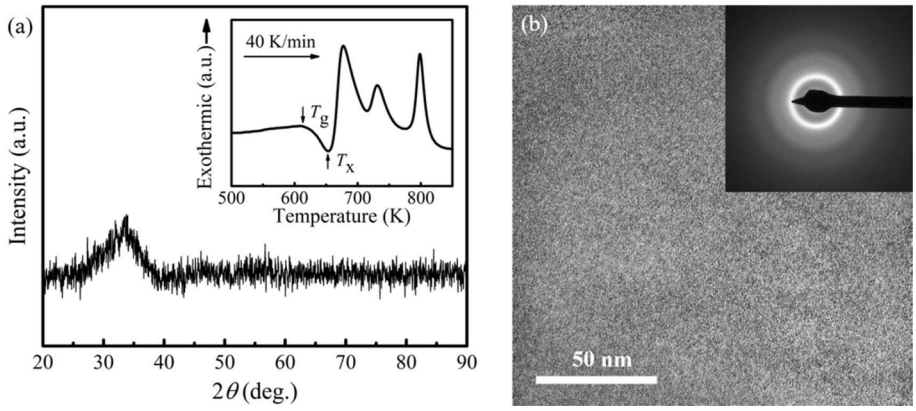

Fig. 1. (a) XRD pattern of the sample. The DSC curve is presented in the inset. (b) Bright-field TEM and the selected area electron diffraction (SAED) pattern.

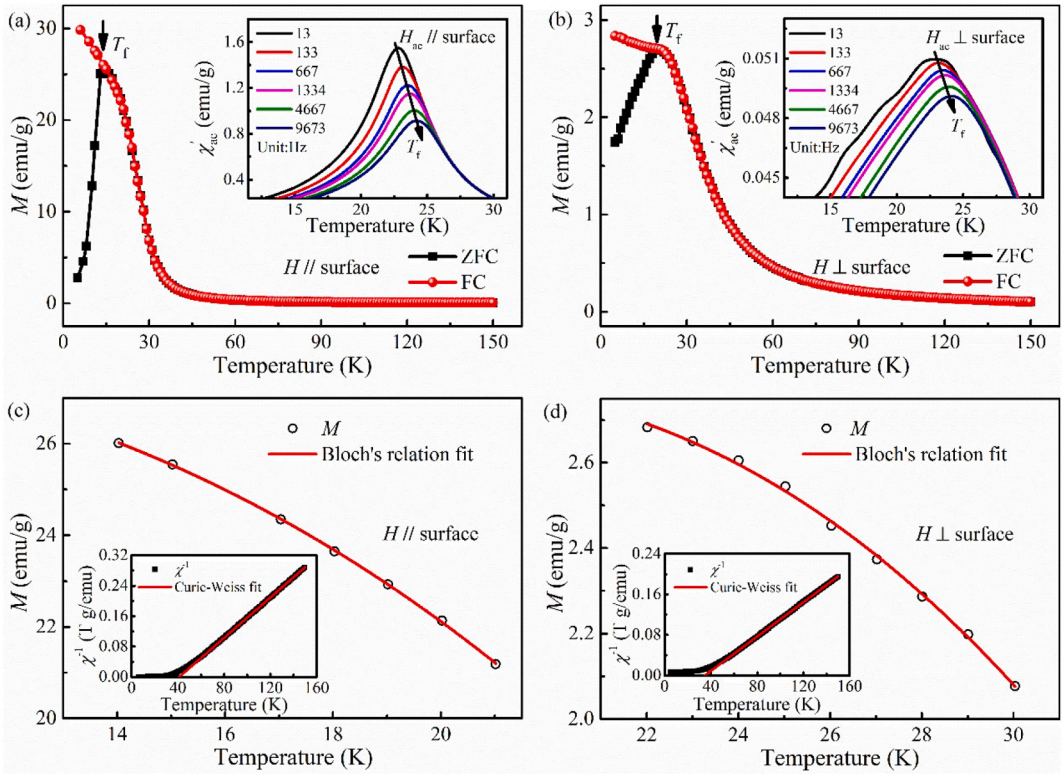

Fig. 2. M_{FC} and M_{ZFC} under field of 0.02 T applied (a) parallel and (b) perpendicular to ribbon surfaces. The insets show the temperature dependent ac susceptibility (real parts) at different frequencies under a fixed excitation field of H_{ac} = 0.0005 T. Temperature dependences of M_{FC} between T_f and T_C and fittings of Bloch's relation for field (c) parallel and (d) perpendicular to ribbon surfaces. Insets show the inverse susceptibility and fittings of Curie-Weiss law well above T_C.

power exponents in different field directions.

2. Experimental

The ingot with a nominal composition of $Gd_{20}Tm_{20}Er_{20}Co_{20}Al_{20}$ was prepared by arc melting pure elements (above 99.9 wt%) in an argon atmosphere and re-melted four times. Present composition was designed by substituting Gd for Dy in $Er_{20}Dy_{20}Co_{20}Al_{20}Tm_{20}$ based on our recent work [33], with the aim to improve the Curie temperature (T_C). Amorphous ribbons with approximate thickness of 30 μm and width of 2 mm were fabricated by single roller melt spinning technique. The amorphous nature was characterized by X-ray diffraction (XRD, Bruker D8 Advance) with Cu Kα radiation, and transmission electron microscopy (TEM, JEM2000ex). Thermal analysis was performed on differential scanning calorimeter (DSC, NETZSCH 404 F3). Magnetic measurements were carried out on a SQUID magnetometer (MPMS, Quantum Design) using sheets with a length of 5 mm, which were cut from the as-spun ribbons. The ac susceptibility and MR were measured by employing a physical properties measurement system (PPMS, Quantum Design 6000). The microstructure was detected using scanning electron microscope (SEM, FEI 3D) equipped with energy dispersive spectroscopy (EDS), and synchrotron XRD with X-ray beam of $3 \times 4.5\ \mu m^2$ in size passed through the sample in transmission mode. The cross section of ribbon for SEM observation was polished.

3. Results and discussion

The amorphous nature of the as-spun $Gd_{20}Tm_{20}Er_{20}Co_{20}Al_{20}$ ribbon is confirmed by the XRD, DSC and TEM characterization. As presented in Fig. 1(a), the XRD pattern shows only a broad hump without any sharp

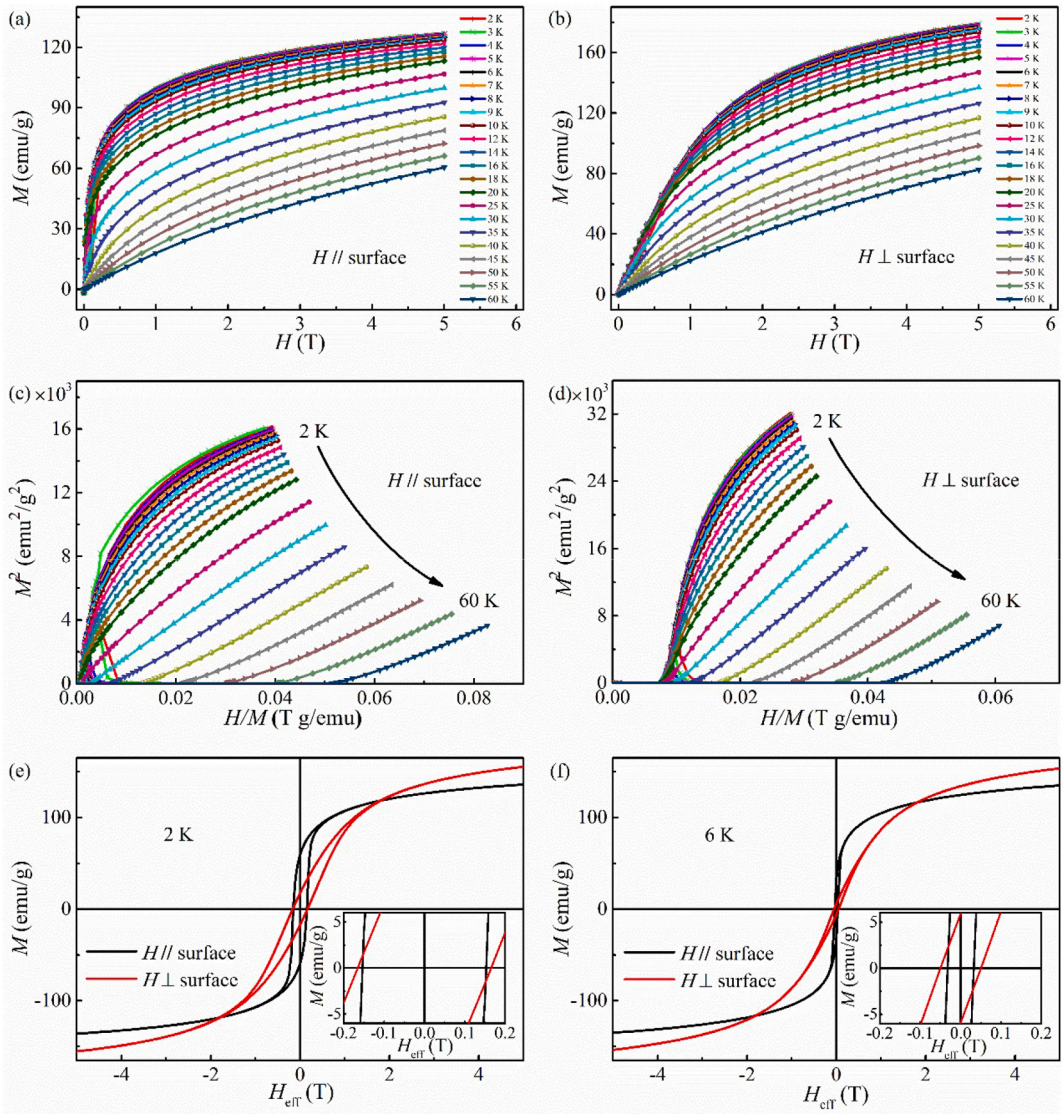

Fig. 3. Isothermal magnetization curves (a-b) and Arrott plots (c-d) for fields parallel and perpendicular to ribbon surfaces. Hysteresis loops after correction of demagnetization effect for parallel and perpendicular fields measured at (e) 2 K and (f) 6 K. Partial enlarged details are given as the insets.

crystalline peak, indicating a fully amorphous structure. The DSC curve manifests a distinct endothermic event with the onset at 623.0 K corresponding to glass transition temperature, T_g, followed by three crystallization exothermic peaks with an onset temperature (T_{x1}) of 660.5 K relevant to primary crystallization. Accordingly, the supercooled liquid region ($\Delta T_x = T_{x1} - T_g$) is determined to be 37.5 K, demonstrating a good glass-forming ability. The bright-field image shown in Fig. 1(b) identifies a uniform structure without any crystalline phase, and in the selected area electron diffraction (SAED) pattern, a single diffraction halo without sharp diffraction rings or dots further verifies the typical amorphous structure.

Temperature dependences of magnetization under parallel (marked by "//") and perpendicular (marked by "⊥") fields with respect to the ribbon surfaces are displayed in Fig. 2(a) and (b), respectively. Here the parallel field is applied along the rolling direction. Both plots exhibit the spin-glass-like freezing behavior [34], viz. the zero-field cooling magnetization (M_{ZFC}) diverges from the field cooling magnetization (M_{FC}) at the temperature where a cusp exists in M_{ZFC}, corresponding to the spin freezing temperature, T_f. The values of T_f under parallel and perpendicular fields are 14.1 and 19.2 K, respectively. The variation of ac susceptibility with temperature was also measured at different frequencies to further reveal the magnetic dynamics. As illustrated in the insets, with increasing frequency from 13 to 9673 Hz, the real parts of the ac susceptibility (χ'_{ac}) manifest peaks at T_f which become weaker and shift towards higher temperatures. The shift of T_f, known as the Mydosh parameter, is calculated by the following equation [35]:

$$\delta T_f = \left[(T_f)_{f_1} - (T_f)_{f_2}\right] \Big/ \left[(T_f)_{f_1}(\log_{10} f_1 - \log_{10} f_2)\right] \quad (1)$$

where $f_1 = 13$ Hz and $f_2 = 9673$ Hz in this work. The Mydosh parameters are determined to be 0.02 and 0.03 for parallel and perpendicular fields, respectively, which are about one order of magnitude smaller than those of 0.1–0.3 for superparamagnets. Therefore, the superparamagnetic transition can be ruled out in present system.

Since sufficient experimental evidence supports that in most RE-based amorphous alloys, Co atoms with concentration below 30 at % do not carry magnetic moments [36], magnetic behaviors of amorphous $Gd_{20}Tm_{20}Er_{20}Co_{20}Al_{20}$ are controlled mainly by RE atoms. On account of the Rudermann-Kittel-Kasuya-Yosida (RKKY) exchange interactions among RE moments dominated by ferromagnetic coupling and the random magnetic anisotropy (RMA) of Tm and Er derived from local electrostatic fields via spin orbit coupling, a transition from paramagnetic to noncollinear-ferromagnetic states is expected above T_f. The large RMA favoring a random orientation of magnetic moment competes

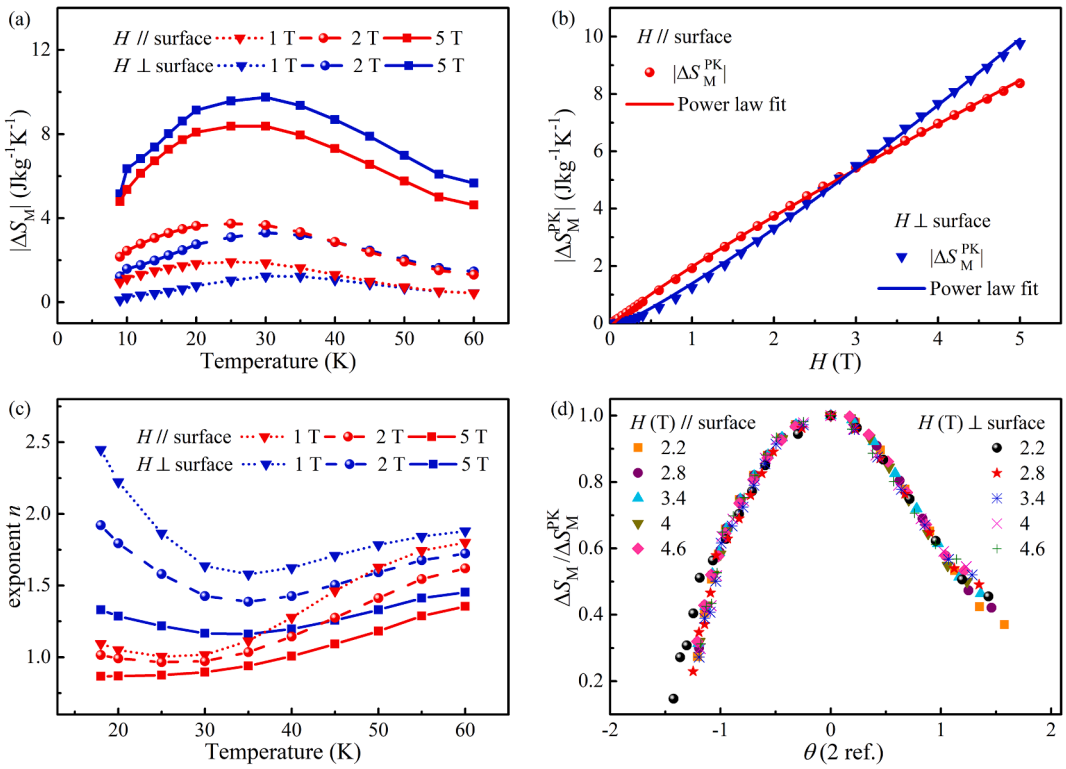

Fig. 4. Temperature dependences of (a) $|\Delta S_M|$ and (c) exponent n for parallel and perpendicular fields of 1 T, 2 T and 5 T. (b) Field dependence of $|\Delta S_M^{PK}|$. (d) Normalized ΔS_M versus rescaled temperature under fields with different magnitudes and orientations.

with ferromagnetic interactions, which forms the noncollinear magnetic structure with finite ferromagnetic correlation length. The lack of long-range ferromagnetic correlation is affirmed by the absence of any positive intercept with $H/M = 0$ axes of Arrott plots [37] displayed in Fig. 3 (c) and (d). From dM_{FC}/dT, T_C of ribbons under parallel and perpendicular fields are determined to be 25.1 and 32.1 K, respectively.

Fig. 2(c) and (d) demonstrates M_{FC} versus temperature between T_f and T_C. The Bloch's relation corrected for thermodynamic effects of spin-wave interactions is adopted for fitting [38]: $M(T) = M(0)(1 - BT^{3/2} - CT^{5/2})$, where B and C are positive numerical coefficients. The B term arises from the simple Bloch theory in which spin waves are treated as noninteracting Bose particles with constant effective mass. The C term corrects the variation of effective mass with velocity. Both plots manifest good fittings with the R-Square above 0.99, indicating the occurrence of spin-wave excitation in the ferromagnetic state. Temperature dependences of the inverse susceptibility and the fittings well above T_C using the Curie-Weiss law: $\chi = C/(T - \Theta)$, where C is the Curie constant [39], are shown in the insets. The Weiss constants Θ, defined as the intercept with the temperature axis by extrapolating the linear part of inverse susceptibility, are determined to be 41.3 and 34.8 K for parallel and perpendicular fields, respectively, confirming the dominated ferromagnetic interactions. The distinct values of Θ in different sample orientations with respect to the field suggest different distributions of exchange interactions.

To evaluate the MCE, two sets of isothermal magnetization curves for ribbons under parallel and perpendicular fields are measured and presented in Fig. 3(a) and (b), respectively. Above T_C, magnetizations of both plots are approximately linear to fields, and below T_C, magnetizations for two mutually orthogonal fields show quite different varying rates with fields especially in the low field ranges. Obviously, the magnetization conducted perpendicularly demonstrates a lower initial susceptibility. It is tempting to recall the demagnetization effect, since ribbons are recognized to generate anisotropic demagnetizing factor. When the field angle increases from 0° to 90° to present ribbon surface, the demagnetizing factor estimated by an analytic expression of rectangular prisms with hypothetical uniform magnetization [40,41], varies from 0.01 to 0.96 in SI units accordingly. In that case, the effective field H_{eff} should be expressed as:

$$H_{eff} = H_{app} - N_D M \quad (2)$$

where H_{app} is the applied field, M is the magnetization and N_D is the demagnetizing factor. However, after correcting the demagnetization effect which works effectively within a limited field of 3 T in Fig. 3(e) and (f), anisotropy of magnetization remains, indicating the existence of additional magnetic anisotropy. And under sufficiently high field, magnetizations measured in perpendicular field are larger than those in parallel field at the same temperature, as illustrated in Fig. 3(a) and (b), which cannot be interpreted by the demagnetization effect.

As a commonly used metric to characterize MCE, ΔS_M can be derived from the Maxwell relation by integrating over the magnetic field [3]:

$$\Delta S_M(T,H) = S_M(T,H) - S_M(T,0) = \int_{H_0}^{H_{max}} \left(\frac{\partial M}{\partial T}\right) dH \quad (3)$$

where H_{max} corresponds to the maximum value of the magnetic field and H_0 is 0 T in this work. Temperature dependences of $|\Delta S_M|$ under different field changes are shown in Fig. 4(a). The magnetic entropy change peak value ($|\Delta S_M^{PK}|$) is obtained at T_{PK} (near T_C), which are estimated to be 25.0 and 30.0 K for parallel and perpendicular fields, respectively. The field orientation plays an important role except for paramagnetic regimes under field changes of 1 and 2 T. Within the field limit of 3 T, the demagnetization effect significantly decreases $|\Delta S_M|$ but weakens in the paramagnetic regime. Maximum $|\Delta S_M|$ values are 9.7 J kg^{-1} K^{-1} under a perpendicular field change of 5 T, and 8.4 J kg^{-1} K^{-1} under the parallel field. Another crucial metric RC [42]: RC $= -\Delta S_M^{PK} \times \delta T_{FWHM}$, where δT_{FWHM} corresponds to the full width at half $-\Delta S_M^{PK}$, are determined to be 551.3 and 458.1 J kg^{-1} under the perpendicular and parallel fields, respectively. A comparison has been made of the magnetocaloric

Table 1
The Curie temperature (T_C), magnetic entropy change peak ($|\Delta S_M^{PK}|$), full width at half $|\Delta S_M^{PK}|$ (δT_{FWHM}) and refrigeration capacity (RC) under a field change of 5 T of $Gd_{20}Tm_{20}Er_{20}Co_{20}Al_{20}$ amorphous ribbon, together with other MCE materials with close T_C reported recently.

Composition	T_C (K)	$\|\Delta S_M^{PK}\|$(J kg^{-1} K^{-1})	δT_{FWHM}(K)	RC (J kg^{-1})	Refs.
$Gd_{20}Tm_{20}Er_{20}Co_{20}Al_{20}$ (⊥)	32.1	9.7	56.8	551.3	This work
$Gd_{20}Tm_{20}Er_{20}Co_{20}Al_{20}$ (//)	25.1	8.4	54.5	458.1	This work
$Gd_{20}Tb_{20}Dy_{20}Co_{20}Al_{20}$	58	9.43	67	632	[23]
$Gd_{20}Tb_{20}Dy_{20}Ni_{20}Al_{20}$	45	7.25	70	507	[23]
$Er_{0.2}Gd_{0.2}Ho_{0.2}Co_{0.2}Cu_{0.2}$	49	11.1	–	806	[24]
$Er_{0.2}Tm_{0.2}Ho_{0.2}Cu_{0.2}Co_{0.2}$	13.5	15.73	–	448.1	[26]
$Er_{20}Dy_{20}Co_{20}Al_{20}Gd_{20}$	43	9.1	68	619	[33]
$Er_{20}Dy_{20}Co_{20}Al_{20}Tb_{20}$	29	8.6	61	525	[33]
$Er_{20}Dy_{20}Co_{20}Al_{20}Tm_{20}$	13	11.9	34	405	[33]
$Ho_{20}Er_{20}Co_{20}Al_{20}Dy_{20}$	18	12.6	37	468	[43]
$Ho_{20}Er_{20}Co_{20}Al_{20}Tm_{20}$	9	15	25	375	[43]
$Gd_{20}Dy_{20}Er_{20}Co_{20}Al_{20}$	42	7.7	–	523	[44]
HoFeAl (compound)	55	6.1	–	311	[8]
ErCoC (compound)	10	18.7	–	371	[8]

properties between the $Gd_{20}Tm_{20}Er_{20}Co_{20}Al_{20}$ alloy and some recently developed MCE materials with close working temperature region, and summarized in Table 1. The $Gd_{20}Tm_{20}Er_{20}Co_{20}Al_{20}$ HE amorphous alloy exhibits a large $|\Delta S_M|$ over a wide temperature range, resulting in a large RC value comparable with those of the other MCE materials, which makes present alloy system attractive for cryogenic magnetic refrigeration.

The $|\Delta S_M^{PK}|$ varying with field is presented in Fig. 4(b). Within the field change range of 0–3 T, $|\Delta S_M^{PK}|$ for the perpendicular field is smaller than that for the parallel field. However, as the field rises continuously, the inverse behavior takes place. Such findings imply different field dependences of $|\Delta S_M|$ for different field orientations. Based on classical exponential expression [32]: $|\Delta S_M| \propto H^n$, temperature-dependent n is obtained and shown in Fig. 4(c). The n values at T_{PK} determined from Fig. 4(b) are 0.9 and 1.2 for parallel and perpendicular fields, respectively. The n value for parallel field is comparable to those of other HE amorphous alloys [28,44,45]. Here the n values are larger under perpendicular field than those under parallel field in the whole investigated temperature range, as a result of the stronger field dependence of magnetization and thus the ΔS_M coming from Maxwell relation. The increase of n should be attributed to the combined effect of the demagnetizing factor [32] and magnetic anisotropy. Besides, normalized $\Delta S_M/\Delta S_M^{PK}$ versus rescaled temperature is shown in Fig. 4(d). Two reference temperatures fulfilling the relation $\Delta S_M(T_{r1} < T_C)/\Delta S_M^{PK} =$

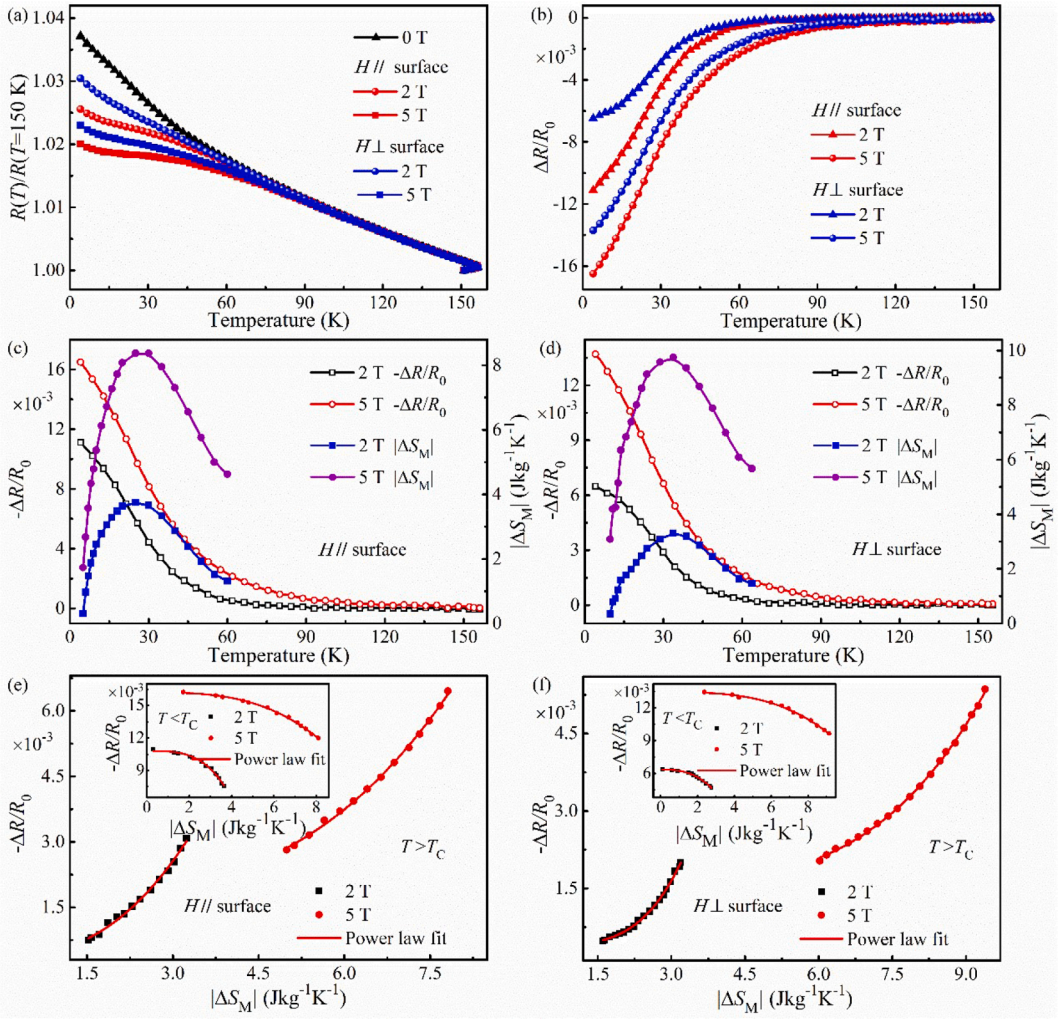

Fig. 5. Temperature dependences of (a) resistance and (b) MR under fields with different magnitudes and orientations. Temperature-dependent MR and ΔS_M under fields of 2 T and 5 T (c) parallel and (d) perpendicular to ribbon surfaces. Correlations between MR and ΔS_M above T_C for fields (e) parallel and (f) perpendicular to ribbon surfaces. Correlations below T_C are shown in insets accordingly.

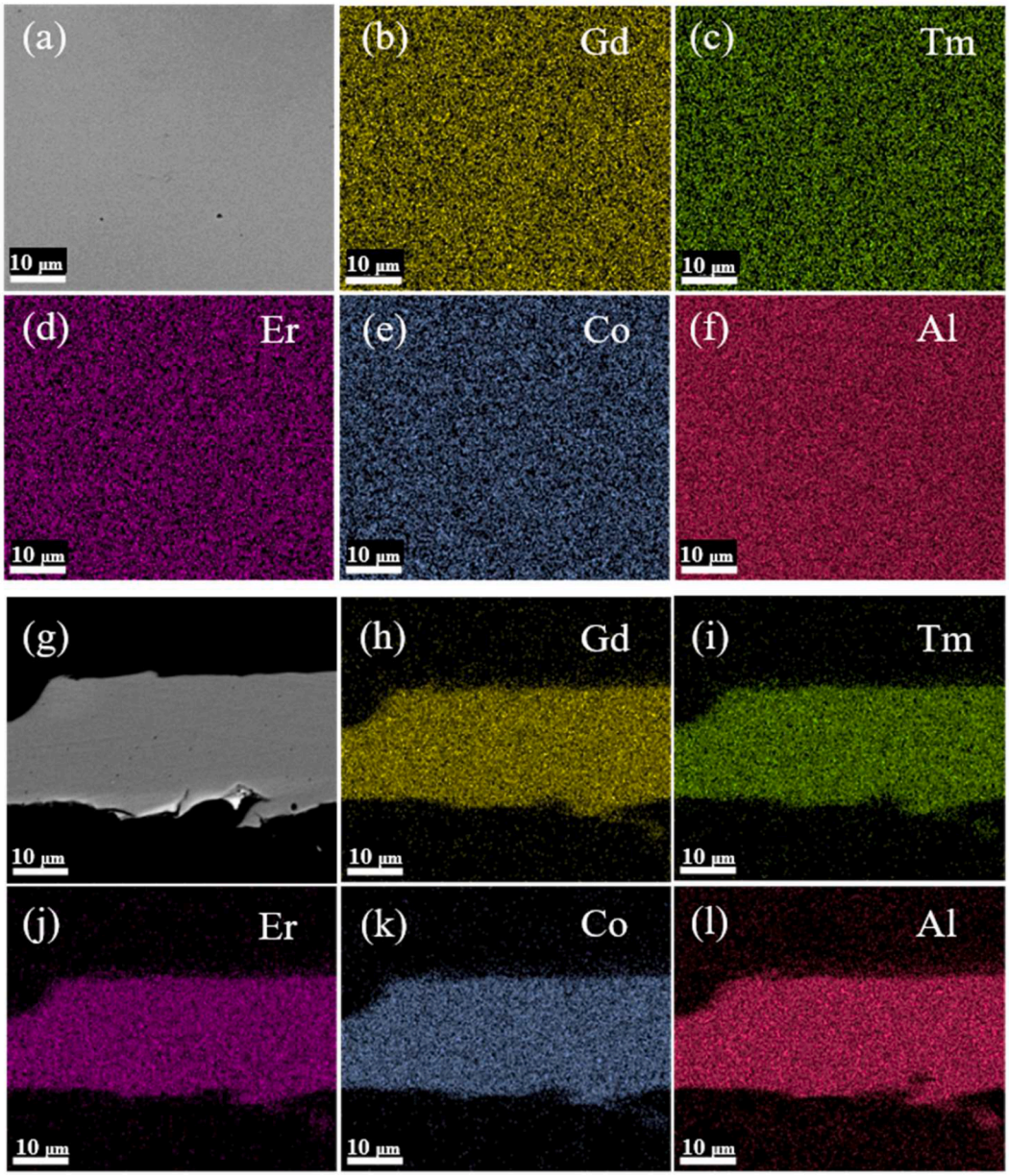

Fig. 6. Typical back-scattered electron (BSE) and EDS mapping images: (a) free surface of the $Gd_{20}Tm_{20}Er_{20}Co_{20}Al_{20}$ ribbon. (b–f) EDS mapping images of Gd, Tm, Er, Co and Al elements of (a), respectively. (g) Cross section of the $Gd_{20}Tm_{20}Er_{20}Co_{20}Al_{20}$ ribbon. (h–l) EDS mapping images of Gd, Tm, Er, Co and Al elements of (g), respectively.

$\Delta S_M(T_{r2} > T_C)/\Delta S_M^{PK} = 0.6$ are selected, to rescale the temperature axis [46,47]:

$$\theta = \begin{cases} -(T - T_C)/(T_{r1} - T_C), & T \le T_C \\ (T - T_C)/(T_{r2} - T_C), & T > T_C \end{cases} \quad (4)$$

The universal curve proves that the demagnetization effect is the main resource of anisotropic field dependence of ΔS_M [32], and that a second-order transition distinguished by positive slopes of Arrott plots [48] in Fig. 3(c) and (d) is indeed responsible for the MCE [49,50].

Fig. 5(a) and (b) depicts temperature-dependent resistances and corresponding MR $(= R_H/R_0 - 1)$ under different fields. For ease comparison, the relative resistance is exhibited. Resistances of present sample show negative temperature coefficients as in many amorphous alloys, and sharp increases at low temperatures. Moreover, the obvious field dependence of resistance is observed, which may come from the Kondo effect [51] and the Coulomb electron-electron interaction effect [52], for which the resistances have $\ln T$ and $\sqrt{T}$ dependences, respectively. But the totally negative MR supports the main Kondo-type contribution to the field dependence of resistance. By applying an external field, the local Kondo coupling which tends to destroy the magnetic correlation is suppressed, leading to the decrease of resistance with increasing field magnitude. In Fig. 5(b), anisotropic negative MR begin roughly at T_C and grow increasingly with decreasing temperature. It may seem anomalous in the HE amorphous alloy with a distinctly high RE content, where strong RKKY interactions are expected. RKKY interactions resulting in consecutive spin-flip scattering of conduction electrons compete against the Kondo effect and favor a resistivity reduction by $-1/T$ at low temperatures, leading to positive MR [51]. The negative MR is presumably set down to the wide distribution of atomic packing [53]. It is noteworthy that at a given field magnitude, the parallel orientation always generates greater MR.

The MR was found to have the similar field/temperature dependence with MCE in some crystalline magnets [54–56]. At present, the

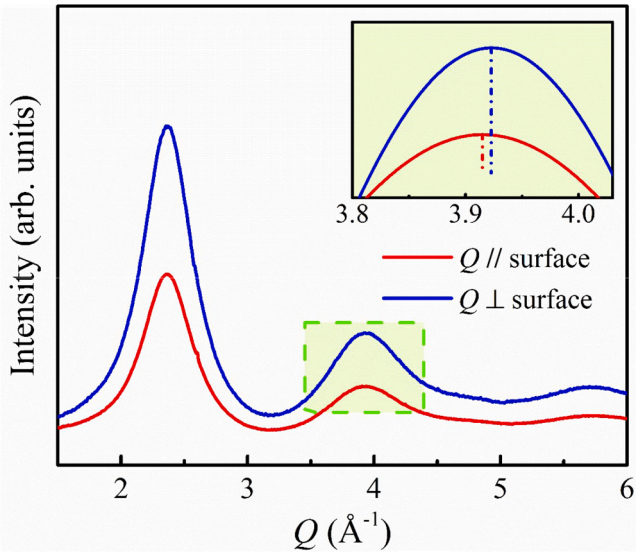

Fig. 7. Synchrotron XRD patterns for scattering vector (Q) directions parallel and perpendicular to the surfaces. Inset is the magnification image of the green rectangular area.

generality in different kinds of magnetocaloric materials has not been achieved. To shed new light on the mechanism of MCE of HE amorphous alloys, the connection between ΔS_M and MR is explored in present system. Fig. 5(c) and (d) presents $-\Delta R/R_0$ and $|\Delta S_M|$ varying with temperature under parallel and perpendicular fields, respectively. Strikingly, $-\Delta R/R_0$ and $|\Delta S_M|$ in both plots share similar temperature dependences above T_C. Whereas, values of $-\Delta R/R_0$ rise continuously with decreasing temperature below T_C, which is different from that of $|\Delta S_M|$. It was reported that $-\Delta R/R_0$ showed similar temperature dependence with $|\Delta S_M|$ for the amorphous ferromagnet $Gd_{46}Co_{19}Al_{29}B_6$, both presenting a peak [57]. The lack of a peak in MR for $Gd_{20}Tm_{20}Er_{20}Co_{20}Al_{20}$ may be associated with the strong RMA and spin-glass-like state at low temperatures. It is demonstrated that MR reflects a complicated mechanism involving spin contribution and orbit contribution [57], which is more complex than ΔS_M. Significantly, MR and ΔS_M reveal a power law correlation under different fields: $MR \propto |\Delta S_M|^c$, as indicated in Fig. 5(e) and (f). In the temperature range of $T > T_C$, the values of c for 2 T (5 T) are determined to be 2.5 (3.2) and 4.0 (4.3) in parallel and perpendicular fields, respectively. And in the low temperature range of $T < T_C$, values of c are 3.4 (3.0) and 2.7 (3.2), respectively. Similar power-law correlation was observed around and below the magnetic ordering temperature in an Er-based amorphous alloy with spin-glass-like freezing behavior [58]. In contrast, Gd-based amorphous alloys with the paramagnetic-ferromagnetic transition were found to have the linear relation below T_C [57,59]. The magnetic configuration seems to have an important effect on this kind of correlation. The underlying mechanism of the MR-MCE correlation remains unclear, the understanding of which requires more theoretical and experimental investigations.

To explore the possible structural origin of the anisotropy of magnetization, MCE and MR performances, SEM and synchrotron XRD experiments were further conducted. Fig. 6(a) and (g) show the back-scattered electron (BSE) images taken from the surface and cross section of the ribbon, respectively, which both reveal an amorphous structure. The dark features superimposing the homogenous background are certified to be the surface irregularity and the internal defect coming from the preparation process, respectively. EDS mapping images indicate that each elemental distribution is even for both the surface and cross section. Therefore, it is interpreted from the results that the microstructure and composition of both the surface and cross section of the ribbon are homogeneous, without the existence of crystalline phases or distinct surface features causing the magnetic anisotropy.

The synchrotron XRD was carried out with scattering vector (Q) parallel and perpendicular to the ribbon surface, and the corresponding patterns are displayed in Fig. 7. The absence of sharp diffraction peaks further confirms the amorphous nature, and rules out the magnetic anisotropy caused by crystallization. The position of the first peak around 2.365 Å^{-1} remains almost the same for different measuring directions. But the full width at half maximum (FWHM) of the peak does show clear difference for Q directions parallel and perpendicular to the surface, with FWHM values of 0.480 and 0.482 Å^{-1}, respectively. It suggests a wider distribution of the interatomic spacing and thus a higher degree of disordering along the Q direction perpendicular to the surface [60,61]. The structural anisotropy is further reflected by the position of second peak. As illustrated by the inset for the enlarged part, the second peak for Q direction perpendicular to the surface shifts to a higher Q-position relative to that parallel to the surface, with a difference of 0.008 Å^{-1}. These results clearly indicate the anisotropy feature of the packing of short-range/medium-range orders in present HE amorphous ribbon. The magnetic interactions (such as dipolar [62] and RKKY interactions) involving these anisotropically distributed atomic pairs (like the RE-RE pairs) may behave in an anisotropic manner, which thus causes the observed anisotropy of magnetization, MCE and MR. Under the high perpendicular field, the enhanced ferromagnetic interactions associated with a favored distribution of interatomic distances for RE-RE pairs may contribute to the higher magnetization and thus the greater MCE. More investigations are needed to further clarify this in the future.

4. Conclusion

To summary, the coexistence of magnetic anisotropy and demagnetization effect in $Gd_{20}Tm_{20}Er_{20}Co_{20}Al_{20}$ HE amorphous ribbon results in anisotropic magnetization, MCE and MR. The anisotropic microstructure, associated with the anisotropic distributions of RE-RE (Co) distances, may contribute to the magnetic anisotropy. For the ribbon sample measured in a perpendicular field, the greater MCE is related to the higher magnetization, which may be due to the enhanced exchange interactions coming from the favored distributions of interatomic distance. In addition, the power law correlation between MR and ΔS_M shows different power exponents in parallel and perpendicular fields with respect to the ribbon surface, which can guide the development of advanced magnetocaloric amorphous alloys.

CRediT authorship contribution statement

Mingjuan Cai: Conceptualization, Methodology, Formal analysis, Investigation, Visualization, Writing - original draft. **Qiang Luo:** Conceptualization, Methodology, Writing - review & editing. **Qiaoshi Zeng:** Resources. **Baolong Shen:** Supervision, Resources, Formal analysis, Writing - review & editing.

Declaration of Competing Interest

The authors declare that they have no known competing financial interests or personal relationships that could have appeared to influence the work reported in this paper.

Acknowledgments

This work was supported by the National Natural Science Foundation of China (Grant Nos. 51631003 and 51971061) and the Fundamental Research Funds for the Central Universities (Grant No. 2242020R1003).

References

[1] C. Zimm, A. Jastrab, A. Sternberg, V. Pecharsky, K. Gschneidner Jr., M. Osborne, I. Anderson, Adv. Cryog. Eng. 43 (1998) 1759.
[2] V. Pecharsky, K. Gschneidner Jr., Int. J. Refrig. 29 (2006) 1239.
[3] M. Balli, S. Jandl, P. Fournier, A. Kedous-Lebouc, Appl. Phys. Rev. 4 (2017), 021305.
[4] L. Li, Y. Yuan, Y. Qi, Q. Wang, S. Zhou, Mater. Res. Lett. 6 (2018) 67.
[5] L. Li, P. Xu, S. Ye, Y. Li, G. Liu, D. Huo, M. Yan, Acta Mater. 194 (2020) 354.
[6] S. Mondal, P. Dutta, S. Chatterjee, S. Giri, S. Majumdar, J. Magn. Magn. Mater. 505 (2020), 166674.
[7] Y. Zhang, J. Alloys Compd. 787 (2019) 1173.
[8] L. Li, M. Yan, J. Alloys Compd. 823 (2020), 153810.
[9] F. Yuan, J. Du, B.L. Shen, Appl. Phys. Lett. 101 (2012), 032405.
[10] P. Jia, L. Duan, K. Wang, E. Wang, J. Mater. Sci. Technol. 35 (2019) 2283.
[11] B.G. Shen, J.R. Sun, F.X. Hu, H.W. Zhang, Z.H. Cheng, Adv. Mater. 21 (2009) 4545.
[12] L. Xia, Q. Guan, D. Ding, M.B. Tang, Y.D. Dong, Appl. Phys. Lett. 105 (2014), 192402.
[13] Q. Luo, D.Q. Zhao, M.X. Pan, W.H. Wang, Appl. Phys. Lett. 90 (2007), 211903.
[14] L.M. Moreno-Ramírez, V. Franco, A. Conde, H. Neves Bez, Y. Mudryk, V. K. Pecharsky, J. Magn. Magn. Mater. 457 (2018) 64.
[15] B.Z. Tang, P. Yu, D. Ding, C. Wu, L. Xia, J. Magn. Magn. Mater. 424 (2017) 275.
[16] H.F. Belliveau, Y.Y. Yu, Y. Luo, F.X. Qin, H. Wang, H.X. Shen, J.F. Sun, S.C. Yu, H. Srikanth, M.H. Phan, J. Alloys Compd. 692 (2017) 658.
[17] Q. Luo, M. Tang, J. Shen, J. Magn. Magn. Mater. 401 (2016) 406.
[18] F. Otto, Y. Yang, H. Bei, E.P. George, Acta Mater. 61 (2013) 2628.
[19] Z. Zhang, M.M. Mao, J. Wang, B. Gludovatz, Z. Zhang, S.X. Mao, E.P. George, Q. Yu, R.O. Ritchie, Nat. Commun. 6 (2015) 10143.
[20] Y. Zhang, T.T. Zuo, Z. Tang, M.C. Gao, K.A. Dahmen, P.K. Liaw, Z.P. Lu, Prog. Mater. Sci. 61 (2014) 1.
[21] W.H. Wang, JOM 66 (2014) 2067.
[22] J. Kim, H.S. Oh, J. Kim, C.W. Ryu, G.W. Lee, H.J. Chang, E.S. Park, Acta Mater. 155 (2018) 350.
[23] J. Huo, L. Huo, H. Men, X. Wang, A. Inoue, J. Wang, C. Chang, R.W. Li, Intermetallics 58 (2015) 31.
[24] L. Li, C. Xu, Y. Yuan, S. Zhou, Mater. Res. Lett. 6 (2018) 413.
[25] L. Xue, L. Shao, Q. Luo, B.L. Shen, J. Alloys Compd. 790 (2019) 633.
[26] Z. Dong, Z. Wang, S. Yin, Intermetallics 124 (2020), 106879.
[27] Y. Yuan, Y. Wu, X. Tong, H. Zhang, H. Wang, X.J. Liu, L. Ma, H.L. Suo, Z.P. Lu, Acta Mater. 125 (2017) 481.
[28] W. Sheng, J. Wang, G. Wang, J. Huo, X. Wang, R. Li, Intermetallics 96 (2018) 79.
[29] K. Wu, C. Liu, Q. Li, J. Huo, Y. Sun, J. Magn. Magn. Mater. 489 (2019), 165404.
[30] R. Caballero-Flores, V. Franco, A. Conde, L.F. Kiss, J. Appl. Phys. 105 (2009) 07A919.
[31] A.F. Manchon-Gordon, J.J. Ipus, L.M. Moreno-Ramirez, J.S. Blazquez, C.F. Conde, V. Franco, A. Conde, J. Alloys Compd. 765 (2018) 437.
[32] C. Romero-Muñiz, J.J. Ipus, J.S. Blázquez, V. Franco, A. Conde, Appl. Phys. Lett. 104 (2014), 252405.
[33] J. Li, L. Xue, W. Yang, C. Yuan, J. Huo, B.L. Shen, Intermetallics 96 (2018) 90.
[34] Q.Y. Dong, B.G. Shen, J. Chen, J. Shen, F. Wang, H.W. Zhang, J.R. Sun, J. Appl. Phys. 105 (2009), 053908.
[35] P. Bag, P.R. Baral, R. Nath, Phys. Rev. B 98 (2018), 144436.
[36] J. Du, Q. Zheng, E. Brück, K.H.J. Buschow, W.B. Cui, W.J. Feng, Z.D. Zhang, J. Magn. Magn. Mater. 321 (2009) 413.
[37] J.S. Kouvel, M.E. Fisher, Phys. Rev. 136 (1964) A1626.
[38] F.J. Dyson, Phys. Rev. 102 (1956) 1230.
[39] E. Petrovsky, A. Kapicka, J. Geophys. Res. 111 (2006) B12S27.
[40] B. Schwarz, N. Mattern, J.D. Moore, K.P. Skokov, O. Gutfleisch, J. Eckert, J. Magn. Magn. Mater. 323 (2011) 1782.
[41] A. Aharoni, J. Appl. Phys. 83 (1998) 3432.
[42] K.A. Gschneidner Jr., V.K. Pecharsky, Annu. Rev. Mater. Sci. 30 (2000) 387.
[43] J. Huo, L. Huo, J. Li, H. Men, X. Wang, A. Inoue, C. Chang, J.Q. Wang, R.W. Li, J. Appl. Phys. 117 (2015), 073902.
[44] L. Xue, Q. Luo, L. Shao, B.L. Shen, J. Magn. Magn. Mater. 497 (2020), 166015.
[45] J. Huo, J. Wang, W.H. Wang, J. Alloys Compd. 776 (2019) 202.
[46] V. Franco, A. Conde, J.M. Romero-Enrique, J.S. Blázquez, J. Phys.: Condens. Matter 20 (2008), 285207.
[47] V. Franco, A. Conde, Int. J. Refrig. 33 (2010) 465.
[48] B.K. Banerjee, Phys. Lett. 12 (1964) 16.
[49] V. Franco, A. Conde, V. Provenzano, R.D. Shull, J. Magn. Magn. Mater. 322 (2010) 218.
[50] C.M. Bonilla, J. Herrero-Albillos, F. Bartolomé, L.M. García, M. Parra-Borderías, V. Franco, Phys. Rev. B 81 (2010), 224424.
[51] J. Ruvalds, Q.G. Sheng, Phys. Rev. B 37 (1988) 1959.
[52] P.A. Lee, T.V. Ramakrishnan, Rev. Mod. Phys. 57 (1985) 287.
[53] H.B. Ke, J.F. Zeng, C.T. Liu, Y. Yang, J. Mater. Sci. Technol. 30 (2014) 560.
[54] R. Rawat, I. Das, J. Phys.: Condens. Matter 13 (2001) L379.
[55] J.C.P. Campoy, E.J.R. Plaza, A.A. Coelho, S. Gama, Phys. Rev. B 74 (2006), 134410.
[56] N. Sakamoto, T. Kyomen, S. Tsubouchi, M. Itoh, Phys. Rev. B 69 (2004), 092401.
[57] Q. Luo, J. Shen, Intermetallics 92 (2018) 79.
[58] X. Kou, Q. Luo, P.N. Dinh, J. Shen, J. Alloys Compd. 699 (2017) 591.
[59] J. Zhu, Q. Luo, M. Cai, B. Ji, B.L. Shen, J. Magn. Magn. Mater. 507 (2020), 166828.
[60] S. Michalik, J. Durisin, D. Balga, K. Saksl, M. Durisin, M. Drakopoulos, J. Alloys Compd. 687 (2016) 188.
[61] S. Michalik, J. Michalikova, M. Pavlovic, P. Sovak, H.-P. Liermann, M. Miglierini, Acta Mater. 80 (2014) 309.
[62] T. Mizoguchi, G.S. Cargill, J. Appl. Phys. 50 (1979) 3570.